Wettability and CHF limits of Accident-Tolerant nuclear fuel cladding materials in light water reactor conditions

Preprint submitted to

Applied Thermal Engineering

Wettability and CHF limits of Accident-Tolerant Nuclear Fuel Cladding Materials in Light Water Reactor Conditions

G.Y. Su[1], T. A. Moreira[2], D. Lee[2], A. Jena[1], G. Wang[3], A. Byers[3], B. Phillips[1], Z. Karoutas[3], M. Anderson[2], M. Bucci[1]

1 Department of Nuclear Science and Engineering, Massachusetts Institute of Technology, Cambridge, MA 02139, USA

2 Department of Mechanical Engineering, University of Wisconsin–Madison, 1500 Engineering Drive, Madison, WI 53706, United States

3 Westinghouse Electric Company LLC, Columbia, SC 29223

ABSTRACT

We present the results of experimental investigations aimed at evaluating the thermal-hydraulic performance of chromium-coated zircaloy, i.e., one of the most promising accident tolerant fuel (ATF) cladding material for light water nuclear reactors. Precisely, we investigate the wettability and critical heat flux (CHF) limits of chromium-coated and conventional zircaloy surfaces in prototypical reactor conditions. For both surface types, we measure the contact angle in a vapor-saturated atmosphere from ambient pressure to the operating pressure of pressurized water reactors (PWRs), i.e., ~15 MPa. We measure the ambient-pressure steady-state flow boiling CHF with a spatially uniform heat flux. We measure the high-pressure steady-state flow boiling CHF with a cosine shape heat flux (up to 20 MPa) and with a uniform heat flux (up to 15 MPa), also exploring the effect of CRUD deposits on the chromium-coated surface. Our results reveal that the chromium surface and the bare zircaloy surface have similar wettability and both become super-hydrophilic in PWR conditions, and that there is practically no difference in the steady-state CHF limits, both at low-pressure and high-pressure conditions, also when the chromium-coated surface is covered by a CRUD deposit. However, while the chromium-coating does not improve the CHF compared to the bare zircaloy surface, it improves the post-CHF behavior. The chromium coating prevents the reaction between zircaloy and steam, which results in the formation of a brittle zirconium oxide through the surface of the cladding. We also measure the transient CHF under exponentially escalating heat flux inputs of a nano-smooth and a rough surface mimicking a chromium-coated zircaloy cladding. Interestingly, the results of the transient heat flux tests suggest that the CHF limit for very short periods (i.e., fast transients) is independent of the surface finish, being the same for a rough chromium surface or a nano-smooth surface.

Keywords

CHF, wettability, contact angle, high-pressure, nuclear fuel cladding, zircaloy, chromium, ATF, LWR, RIA

1. Introduction

Since the 2011 Fukushima accident, significant research has been devoted to developing accident-tolerant fuel (ATF) cladding materials [1,2]. These investigations have mainly focused on the ability of potential ATF materials to resist runaway steam oxidation under extreme temperature (> 1200 °C) and retain their mechanical strength and structural integrity under thermal shocks [3-5]. However, knowledge of the thermal-hydraulic performance of ATF materials is relatively lacking, particularly under light water reactor (LWR) operating conditions. Precisely, there is an urgent need to clarify whether ATF materials could lead to a deterioration of the CHF limit compared to traditional zirconium alloy (i.e., zircaloy) claddings, as the CHF limit determines, among other factors, the thermal power of LWRs [6].

In pressurized water reactors (PWRs), for instance, water enters the core highly subcooled, and while its bulk temperature does not reach saturation conditions, subcooled nucleate boiling may occur on the fuel claddings in the upper part of the core. This subcooled nucleate boiling regime is very effective. However, the risk of a transition from a nucleate boiling to a film boiling regime (i.e., the departure from nucleate boiling, DNB) is a major concern in the operation of PWRs, as it may also result in the melting of the fuel cladding. Such transition occurs if the local heat flux exceeds the CHF limit. However, while there are several pool and flow boiling CHF studies on zircaloys, the number of studies addressing the CHF performance of ATF materials is still low and limited to low-pressure conditions [7-12]. To support the successful rollout of ATF cladding materials, it is important to thoroughly investigate the CHF limit of these materials and understand how they compare to zircaloys, especially in LWRs conditions.

It is widely recognized that the CHF limit depends on operating conditions (e.g., pressure, temperature, and flow rate, if any) and surface properties. Surface wettability (i.e., surface contact angle with liquid) is known to be a dominant factor, at least in pool boiling at low pressure [13-17]. Higher surface wettability can increase the CHF by affecting the boiling dynamics (e.g., by reducing the bubble departure radius and increasing the bubble departure frequency). Since the wettability is directly correlated to the surface tension and thus a strong function of temperature, it is essential yet very challenging to measure the surface wettability of fuel cladding materials in LWR conditions. There is hitherto no systematic measurement of contact angles on traditional zircaloy up to such high pressure and temperature in vapor-saturated atmospheres, let alone ATF materials. Most measurements were obtained at near atmospheric pressure, and low temperatures [7-12, 18-24]. Only a few studies were performed in pressurized conditions, but in an inert gas environment, which leads to strong evaporation effect especially under elevated temperature conditions [25-27]. Practically, contact angles values input in thermal-hydraulics models used for LWR analyses often rely on data and correlations developed in non-prototypical conditions, or hypothesis on the presumed surface wettability trends [28].

Other than normal steady state conditions, CHF under transient conditions is another major concern in nuclear reactors. Such off-normal scenario might be caused if a rapid insertion of reactivity (e.g., an accidental removal of control rods from the core) leads the nuclear reactor to a prompt-critical state (i.e., a reactivity-initiated accident, or RIA). Under such conditions, the reactor power, $\dot{Q}$, may increase exponentially, i.e., $\dot{Q} \propto e^{t/\tau}$. Depending on the reactivity value, the exponential period τ can vary from a few millisecond (for large insertion of reactivity) to hundreds of milliseconds (for small insertion of reactivity). The delay between the power escalation and the void feedback (i.e., the boiling of water) may lead to a large increase in the reactor power, potentially triggering a DNB event [29-43]. Thus, it is also key to understand the DNB mechanisms and quantify the CHF limit of ATF materials in transient conditions.

Here, we present the results of a research effort involving Massachusetts Institute of Technology (MIT), University of Wisconsin-Madison (UWM), and Westinghouse Electric Company LLC (WEC). This research effort has focused on investigating the thermal-hydraulic performance of chromium coated zircaloy as a candidate ATF cladding concept. Figure 1 shows the general structure of the present research project (in blue) and expected future works (in orange).

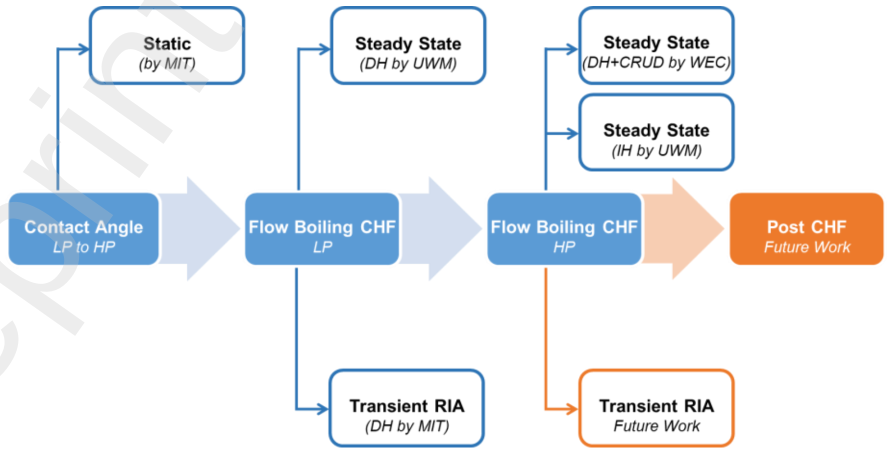

Figure 1. Structure of the research effort. The blue color indicates the investigations discussed in this manuscript, whereas the orange color indicates future research directions.

Precisely, we discuss methodology and results of experimental investigations aimed at characterizing the wettability and CHF limits in low pressure conditions (including transient power escalations) and high-pressure conditions (up to 20 MPa). The wettability of the selected materials is characterized using a special autoclave designed and built by MIT to measure the contact angles of water in a vapor-saturated environment up to the critical pressure of water. Low-pressure (LP), steady-state CHF flow boiling tests on actual fuel claddings samples are conducted by UWM. Transient CHF tests with power escalation periods ranging from 5 to 500 ms are conducted by MIT using a cladding-simulant heater. High-pressure flow boiling tests are conducted by both UWM and WEC. WEC investigates CHF with uniform heat flux profiles, also considering the effect of CRUD deposits on the surface of the cladding. UWM investigate CHF with a cosine-shape heat flux mimicking the axial heat flux distribution of PWRs.

2. Surface wettability

2.1. High temperature high pressure autoclave facility

Figure 2 shows the MIT high-pressure autoclave facility and the optical setup. This facility allows measuring the contact angle between a liquid droplet and a surface in a vapor-saturated environment (i.e., without noncondensable gases), from ambient to critical pressure conditions. The autoclave features a cruciform geometry. The test sample is accommodated on a stage installed at the crossing joint of the autoclave, aligned with the axis of two sapphire windows that enable optical access to it.

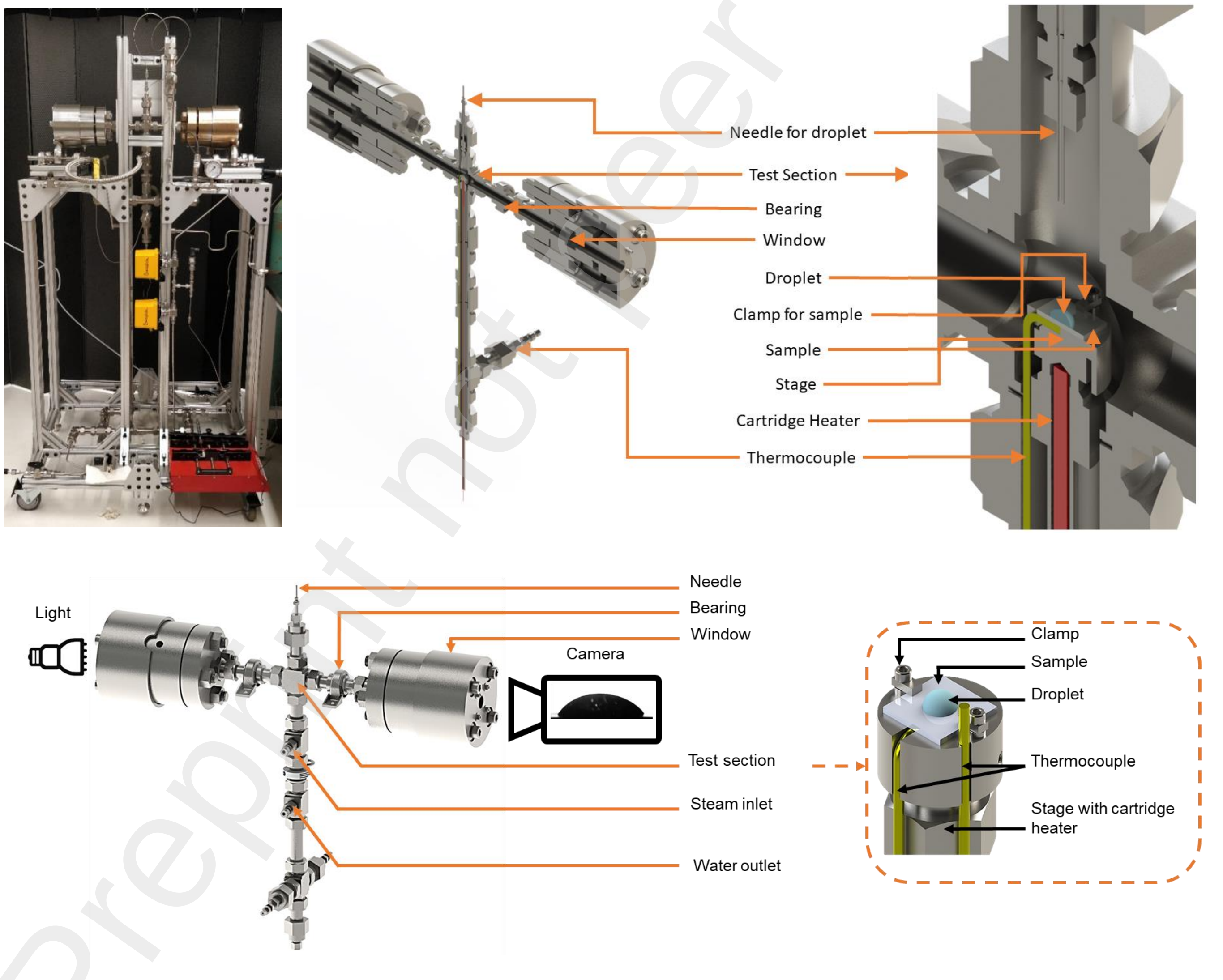

Figure 2. High temperature high-pressure test facility and experimental setup for contact angle measurements at MIT.

Two K-type thermocouples (shown in yellow in Fig. 2) are used to measure the temperatures underneath the test sample and in the vapor atmosphere near it and to verify that they are in equilibrium. The test section can accommodate rectangular samples of different size, from 5 mm × 5 mm to 12.5 mm × 12.5 mm with thickness of 1 to 3 mm. A needle connected to an external syringe pump is used to dispense the droplet on top of the specimen. The needle is in thermal equilibrium with the autoclave atmosphere to ensure that the fluid released from the needle is at the same temperature as the surrounding steam and the sample itself. After a contact angle measurement is made, the surface is flushed with water and a cartridge heater underneath the sample holder is used to evaporate the residual water. Then, the sample is let thermalize before a new droplet is dispensed to make a new measurement. The autoclave pressure and the droplet line pressure are monitored with two pressure transducers separately.

2.2. Experimental procedure

Before its installation in the autoclave, the test sample is solvent-cleaned in a sonicated bath using soapy water, DI water, acetone, ethanol, and DI water again, for seven minutes each. At the beginning of each test, the test facility is purged with argon gas for at least five minutes to remove all the air from the autoclave. Then, the autoclave is vacuumed to remove the non-condensable gas until the pressure drops below 10 kPa and filled with de-aerated DI water to initialize a two-phase equilibrium atmosphere. The autoclave is externally heated using tape heaters, and the temperature and pressure inside the autoclave are carefully controlled and monitored to ensure that thermal equilibrium conditions are attained at the desired pressure setpoint. Once the autoclave has reached equilibrium, a droplet (also in thermal equilibrium) is released from the needle on top of the sample surface.

We measure the static contact angle of deionized (DI) water with selected surfaces using the sessile-drop method, as shown in Fig. 3. We use a high-resolution camera with a resolution of 106 μm/pixel to take backlit images of sessile drops on the sample surface. Then, we use an image processing algorithm to identify the droplet profile and the tangent to this profile at the solid-liquid-vapor contact line. The contact angle value is then calculated from the tangent as shown in Fig. 3. For more details about the image processing technique, the reader is directed to the supplementary material of Ref. [44].

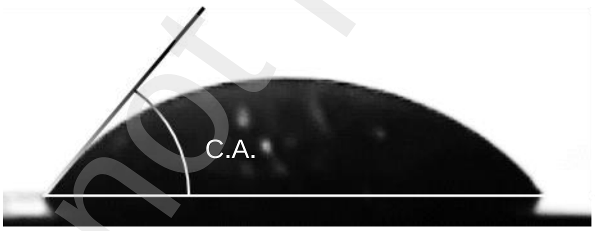

Fig. 3. Illustration of sessile-drop method for static contact angle measurement on smooth Zr-4 surface at T = 213.9 °C, P = 20.6 bar.

Different from tests in inert gas environments, our droplets do not evaporate. They maintain their shape and dimensions for an indefinite period of time. This is possible thanks to the operation in a practically vapor-saturated environment. After each measurement, additional water from the needle is poured to clean the sample surface. Then, the cartridge heater is turned on to evaporate the residual water. After the surface is completely dry, the cartridge heaters are shut down and we wait for the sample to cool down until its temperature stabilizes within ±1°C of the autoclave environment temperature. Then, we repeat the same measurement. At least five measurements are made for each saturation pressure and temperature condition. Then, we change the operating conditions, and collect a new set of measurements. Importantly, we take these measurements for increasing and decreasing pressure and temperature, to explore the possibility of contact angle hysteresis.

2.3. Contact angle measurements

The static contact angle measurements are conducted on two different mirror-polished surfaces, i.e., zircaloy-4 (Zr-4) and chromium. The roughness Ra of the test samples is summarized in

Table 1. The chromium surface is created by coating a mirror polished Zr-4 sample using physical vapor deposition (PVD). The PVD-coated chromium layer is about 1 μm, i.e., it is thick enough to eliminate the impact of Zr-4 substrate on the contact angle [48]. Note that we measure the wettability of mirror polished surfaces with a roughness much lower than commercial surface to eliminate as much as possible surface effects, e.g., due to random roughness, from the analysis. In other words, what we measure here is the intrinsic wettability of the surface.

Table 1. Summary of test samples and the corresponding surface roughness.

Material	Surface finish, Ra [μm]
Zr-4	Mirror-polished, 0.033 ± 0.011
Cr-coated Zr-4	Mirror-polished, 0.050 ± 0.011

Figure 4 (left) shows how the contact angle on the two surfaces change with temperature and pressure. The error bar represents the standard deviation of the contact angle values for the set of five measurements taken at each test condition. Several sub-atmospheric data points for Zr-4 previously obtained by our group (see Kossolapov et al. [45]) are also shown in the plot. The results shown in Figure 4 demonstrate that the contact angle decreases as temperature and pressure increase, which is consistent with the decrease of the liquid-vapor surface tension [46]. Note that, when the contact angle decreases below 20˚, measurements become challenging and inaccurate due to light distortion effects created by the warm vapor in the optical path. Thus, we report the data only until the point when the contact angle is approximately 20˚. However, we have observed that the surfaces become super-hydrophilic above these temperatures (i.e., the droplet spreads over the entire sample surface as soon as it is dispensed, or, in other words, the contact angle is practically 0˚).

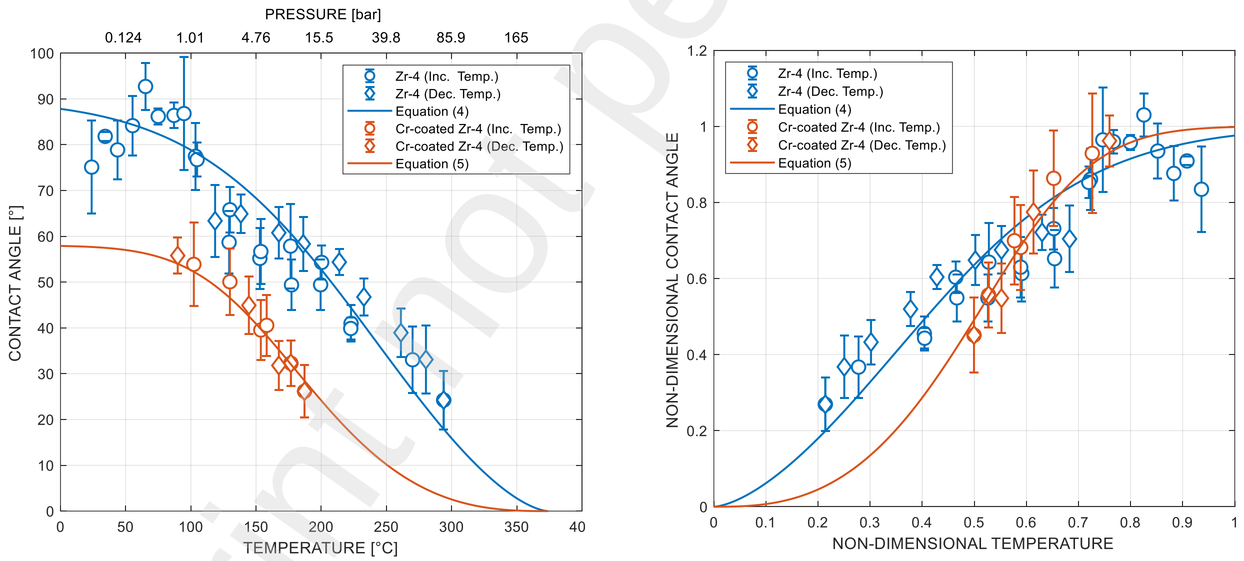

Figure 4. Measured and modeled contact angle versus surface temperature for different test sample materials (left). Comparison of non-dimensional correlation for contact angle versus surface temperature between experimental results and model prediction (right).

The decreasing trend of contact angle versus temperature has implications on the boiling process. It is often argued that the CHF limit depends on the wettability of the boiling surface and that, improving the surface wettability (i.e., decreasing the contact angle), increases the CHF. This statement is mostly supported by many pool boiling data, as wettability effects seem to be less pronounced in flow boiling conditions. However, Zr-4 and chromium have similar contact angles at low temperature conditions, and they both tend to become super-hydrophilic in nuclear reactor conditions, suggesting that a different boiling performance, if any, may not be caused to a wettability effect.

2.4. *Empirical correlations for contact angle*

There have been attempts to model the temperature dependency of contact angle using approaches such as Neumann's theoretical model [46, 47] based on the equation of the state and Adamson's semi-empirical correlation [48]. Unfortunately, there is hitherto no universal model that can accurately capture the temperature dependency of contact angle on different surface materials. In this study, we have chosen a practical approach and developed material-specific empirical correlations for the contact angle of DI water in saturated atmospheres. We define the non-dimensional contact angle θ^* and temperature T^* as follows

$$\theta^* = \frac{\theta}{\theta_0} \tag{2}$$

$$T^* = \frac{T_c - T}{T_c - T_0} \tag{3}$$

Here, θ is the contact angle at any given temperature; θ_0 is the contact angle at 0 °C; T is any given temperature; T_c is critical temperature of water, i.e., 374.15 °C, and T_0 is 0 °C. In configuring the correlation, two widely accepted hypotheses are used, i.e., that a) the contact angle becomes null at the critical point of water and b) the contact angle at 0 °C is approximately the same as at room temperature, i.e., 90˚ for Zr-4 and 58˚ for Cr-coated Zr-4. With these two assumptions, the final form of the contact angle-temperature non-dimensional correlation is obtained by fitting the measured data points with hyperbolic tangent functions. Equations (4) and (5) are the correlations for smooth Zr-4 and chromium, respectively.

$$\theta^* = \tanh\left(2.2\, {T^*}^{1.55}\right) \tag{4}$$

$$\theta^* = \tanh\left(3.5\, {T^*}^{2.70}\right) \tag{5}$$

Dimensional and non-dimensional contact angle values predicted by these correlations are compared to experimental results in Fig.4 (left) and Fig. 4 (right), respectively.

3. Low-pressure, steady-state CHF tests

3.1. *Low-pressure flow boiling test setup*

Figure 5 shows a schematic of the UWM experimental facility (top) and test section (bottom right) for the near-atmospheric, low pressure experiments (i.e., the low-pressure loop). DI water from the reservoir (i.e., a 1.5 m^3 stainless steel tank) is driven through the loop by a centrifugal pump; the frequency of which is controlled by a variable frequency drive (VFD). Downstream the pump the water flows through a Coriolis mass flow meter, a throttling valve (used to mitigate thermal instabilities associated to the bubble nucleation and growth inside the test section during the boiling experiments) and enters the test section. The test section consists of a vertical concentric annular channel (in which the fluid flows upwards), defined by a heater rod (internal boundary) and a glass tube (external boundary), as shown in Figure 1 (bottom right). The rod has a heated length of 456 mm and an outer diameter (OD) of 9.5 mm, while the glass tube has an inner diameter (ID) of 20 mm and is 500 mm long. Centering pins are used to ensure that the heater rod is concentric with the glass tube. During the experiments, the heater rod is directly heated by Joule effect using an 80V-1200A DC power supply. Downstream the test section the water returns to the tank, closing the circuit. To remove the heat added to the water in the loop at the test section and control the temperature in the reservoir, a separate water stream is driven directly from the reservoir through a secondary loop by a VFD-controlled centrifugal pump. In this secondary loop, water flows through a plate-type heat exchanger for heat removal and then returns to the reservoir. On the secondary side of the heat exchanger, a chilled glycol solution provides the ultimate heat sink. Water temperature measurements are performed at the inlet and outlet of the test section through K-type thermocouples. The absolute pressure is measured at the outlet of the test section, and pressure drop across the test channel through a differential pressure transducer. The heater rod is filled with boron nitride to add thermal inertia. It features wall temperature measurements near the end of the heated section (i.e., the location where CHF is expected to occur since the heat flux obtained by Joule heating is uniform) through a K-type thermocouple and axially along the test section length through an optical fiber inserted into a capillary. The disposition of the thermocouple and optical fiber along the cross section of the heater rod is illustrated in Figure 6 (left). The optical fiber temperature measurement technique uses pulsed infrared (IR) light to measure the Rayleigh backscattering from grain boundaries and other random imperfections in a section of standard optical fiber, as illustrated in Figure 6 (right). The optical fiber system has a maximum sampling frequency of 250Hz with a spatial resolution of 2.5 mm. The reader interested in the details of optical fiber temperature measurement is directed to Refs. [12, 49].

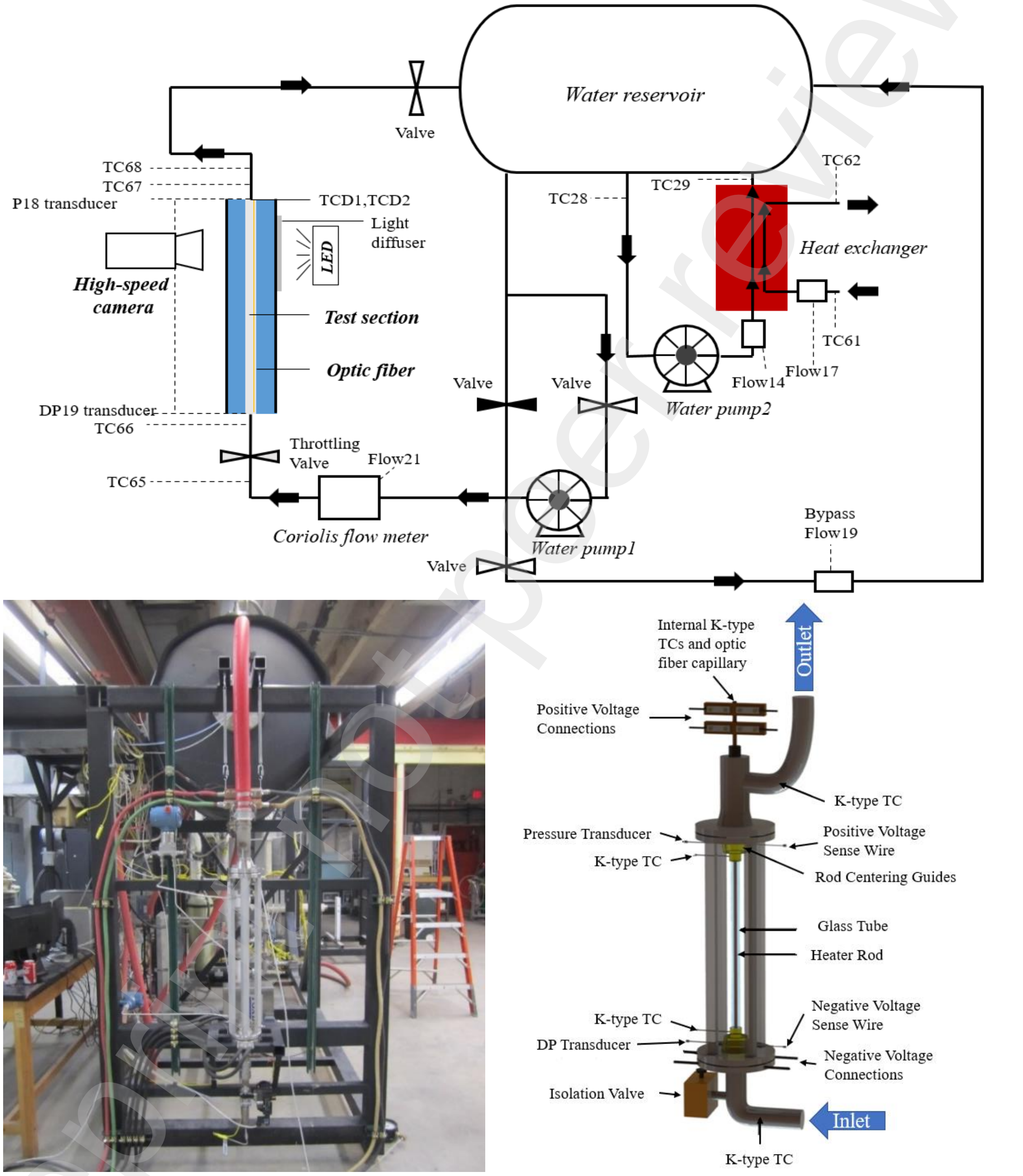

Figure 5. Picture (bottom left) and schematic (top) of the UWM low pressure CHF testing facility and rendering of the test section (bottom right).

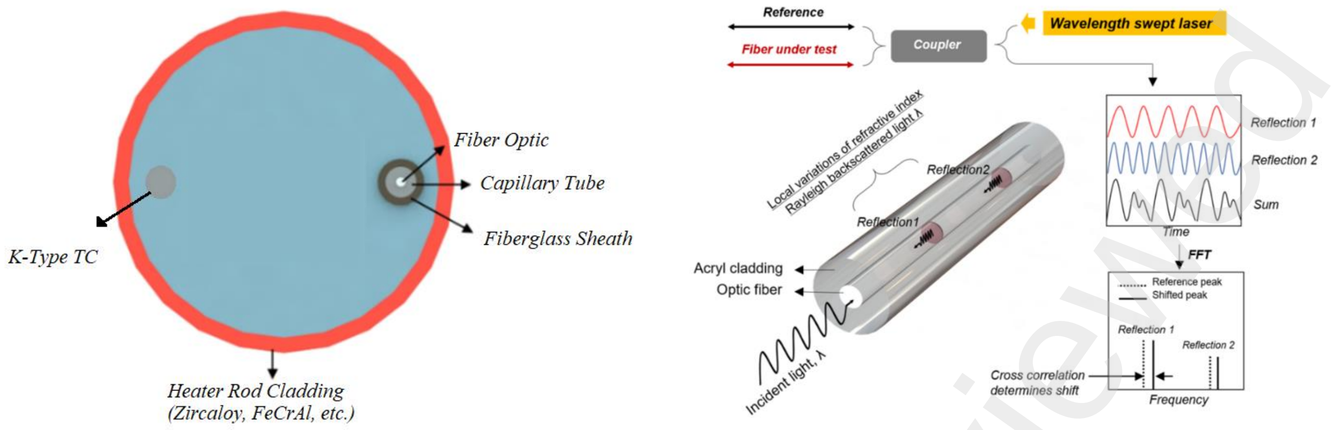

Figure 6. Cross-section view of the heater rod with an embedded optical fiber (left), and illustration of the working principle of the optical fiber temperature measurement (right).

In this study, we test the low-pressure flow boiling CHF limit of heater rods made of four different cladding materials, i.e., bare zircaloy-4, two types (CS-R and CS-S) of cold-sprayed Cr-coated zircaloy, and PVD (Physical Vapor Deposition) Cr-coated zircaloy. CS-R and CS-S have a different surface roughness. CS-S is polished after the cold spray deposition process in order to have a surface roughness similar to one of the bare zircaloy rod. CS-R is instead tested as it is after the cold spray depositions process. The average roughness and the contact angle (of DI water with air at ambient pressure) for each cladding, both measured in a previous study [50], are summarized in Table 2.

Table 2. Summary of the surface properties for all tested rod materials.

Test Material	Ra [µm]	Contact angle [°]
Zircaloy	0.43	75
Cr-Coated Zircaloy (CS-R)	1.22	45
Cr-Coated Zircaloy (CS-S)	0.30	50
Cr-Coated Zircaloy (PVD)	0.45	25

Note that the contact angles on the PVD coated chromium surface is fairly different from the value measured at 1 bar in the high-pressure autoclave. This difference may arise from the gaseous atmosphere, surface finish (as the rod tested here is much rougher), PVD deposition parameters, or contamination of the surface. However, the results in Table 2 seem to show that the cold-sprayed surfaces have very similar wettability, even though CS-R is much rougher than CS-S (note that the suffix R stands for "rough", whereas the suffix S stands for "smooth).

3.2. Test procedure and DNB criterion

The heat flux is gradually increased until departure from nucleate boiling (DNB) occurs. In the early stage of the experiment, the heat flux is increased in steps of 350 kW/m^{2}s. Inlet temperature, pressure and mass flow rate are monitored and compared to their measuring uncertainties to make sure that steady-state conditions are attained at each step. Such a procedure is repeated until the heat flux reaches 1750 kW/m^{2}s. Beyond this point, the heat flux is increased in steps of 1.25 kW/m^2 every 10 seconds until DNB occurs. The DNB is detected by monitoring either the temperature of the boiling surface (measured by the optical fiber and the thermocouple) or the heater rod electrical resistance. As there is only one optical fiber in these low-pressure tests, the optical fiber alone may not timely detect the DNB temperature rise if it occurs in a circumferential location far from it. The same concern exists for the single thermocouple located 25 mm from the end of the heated length. Therefore, the heater rod resistance is employed as an additional indicator to detect the DNB occurrence in these low-pressure tests. The temperature threshold for the DNB detection is ~25 °C above the one at the previous steady-state heat flux step, while the resistance threshold is set at 0.03 Ω above the normal operating resistance of the heater rod. The CHF limit is the heat flux at the last stable step.

3.3. Low-pressure experimental results (near atmospheric conditions)

Low-pressure experiments are performed with an inlet subcooling of 80 °C, a mass flux of 750 $kg/m^2/s$, and an outlet pressure of 116 kPa. For the same type of cladding, experiments are repeated on 2 separate heater rods to reduce random uncertainty and guarantee the repeatability of the results. The measured CHF values from all the tests are plotted in Figure 7, together with AFM (Atomic-Force Microscopy) images of the different surfaces (except CS-S). These results reveal that there is no significant difference in CHF for surfaces with the same roughness, despite the different contact angles (see Table 2). Instead, the CHF on the rougher surface is slightly lower (approximately -10.8%) than the other surfaces. We suspect that the deterioration of the CHF on the rough surface (accompanied by an increase of the boiling heat transfer coefficient) is due to a decrease of the onset of nucleate boiling temperature and an increase of the nucleation site density, consistent with the findings of previous studies from our group [58].

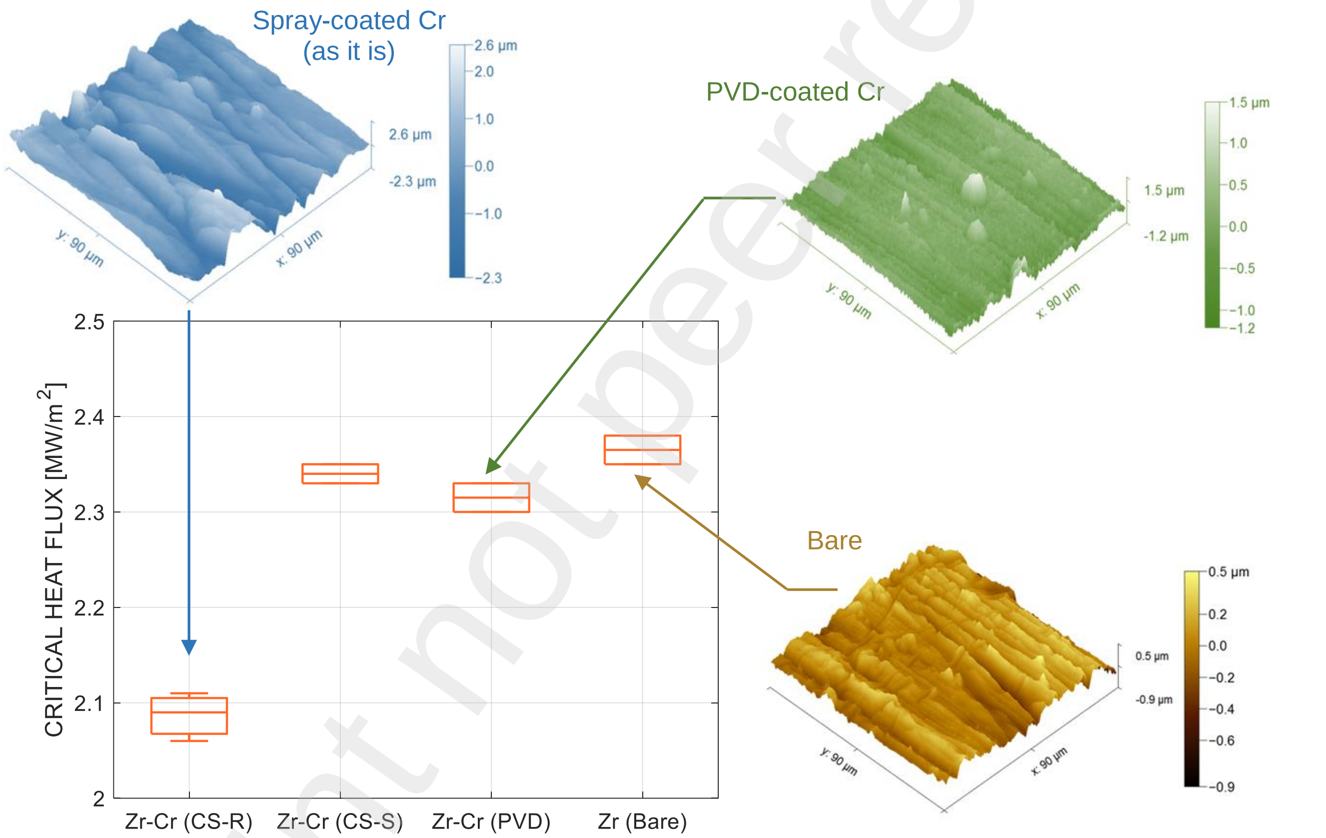

Figure 7. Comparison of measured CHFs from different claddings and AFM images of their surface morphology.

In summary, the results of the low-pressure experiments confirm that the surface wettability has a minor effect in the flow boiling performance. Instead, surface roughness and morphology may play a bigger role, presumably due to their effect on nucleation sites size and density.

4. High-pressure, steady-state CHF tests

High pressure flow boiling tests are performed using two different approaches and experimental facilities. Precisely, the UWM high-pressure flow boiling facility, to explore CHF limits with a cosine shape heat flux distribution obtained using an indirect heating technology, and the Westinghouse WALT loop, which also allows testing the effect of CRUD deposit on the boiling surface, to measure the CHF limit with uniform heat fluxes.

4.1. High-pressure flow boiling experiments with a cosine shape heat flux distribution

Figure 8 shows a schematic and a picture of the UWM high-pressure loop. DI water is driven through the loop by a high-pressure high-temperature centrifugal pump (Chempump™, GCT-5k 36I). Downstream the pump the water flow splits between two branches, one that goes upward through the test section, where the working fluid is heated and boiled, and the other one that by-passes it. Orifice-type mass flow meters are installed in each one of these two branches. After the test section, the two streams merge into a single channel, and flows toward a shell-and-tube heat exchanger. A by-pass valve is used to control the flow rate and, consequently, the heat removed from the working fluid at the heat exchanger in order to control the temperature of the flow at the inlet of the test section. After the heat exchanger, the chilled water stream mixes back with the by-passed stream before returning to the pump. An accumulator with an argon gas plenum is connected to the top region of the loop and it is used to set the system pressure.

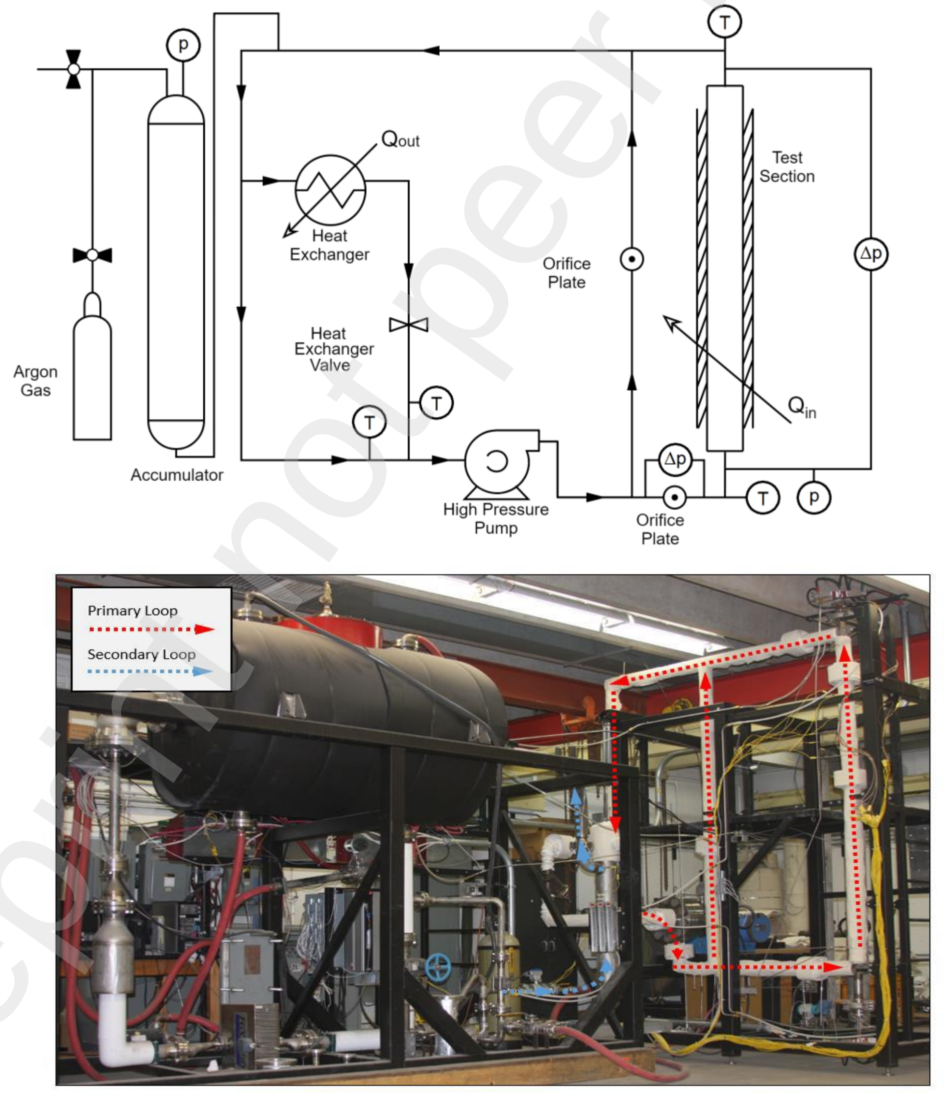

Figure 8. Schematic (top) and picture (bottom) of the UWM high-pressure flow boiling heat transfer test facility.

The high-pressure loop can operate in both subcooled and saturated conditions at maximum pressure and temperature of 25 MPa and 400°C separately. The test section of the high-pressure loop consists of an annular flow channel defined by a heater rod with OD of 9.5 mm and an outer tube of 20 mm ID, similar to the low-pressure one. In this case, however, the heater rod is ~3 m long with a heated length of 2 m, and the outer tube is made of Inconel. The rod is held centered in place though alignment pins distributed along the test section length. The location of these pins is carefully picked to not interfere with the DNB occurrence. The heater rods are designed ad-hoc by Stern lab to provide a cosine heat flux profile that simulates the axial heat flux distribution along an actual LWRs fuel rod. The heat flux distribution follows the equation

$$\frac{q''(x)}{q''_{\mathrm{avg}}} = \theta_0 + \theta_1 \cos\left[2\theta_2\left(\frac{x}{L_{\mathrm{HL}}} - 0.5\right)\right] \tag{6}$$

where $\theta_0 = 0.819$, $\theta_1 = 0.681$, $\theta_1 = 2.436$, q''_{avg} is the average heat flux along the rod, defined by the ratio between the power applied and the area of the heated surface, and L_{HL} represents the total heated length, i.e., 2 m. The cosine profile heat flux is obtained by a specially tailored helical Joule-heating filament made of Inconel 718 (illustrated in Figure 9 (top)) to heat up the heater rod cladding via thermal conduction from the internal surface.

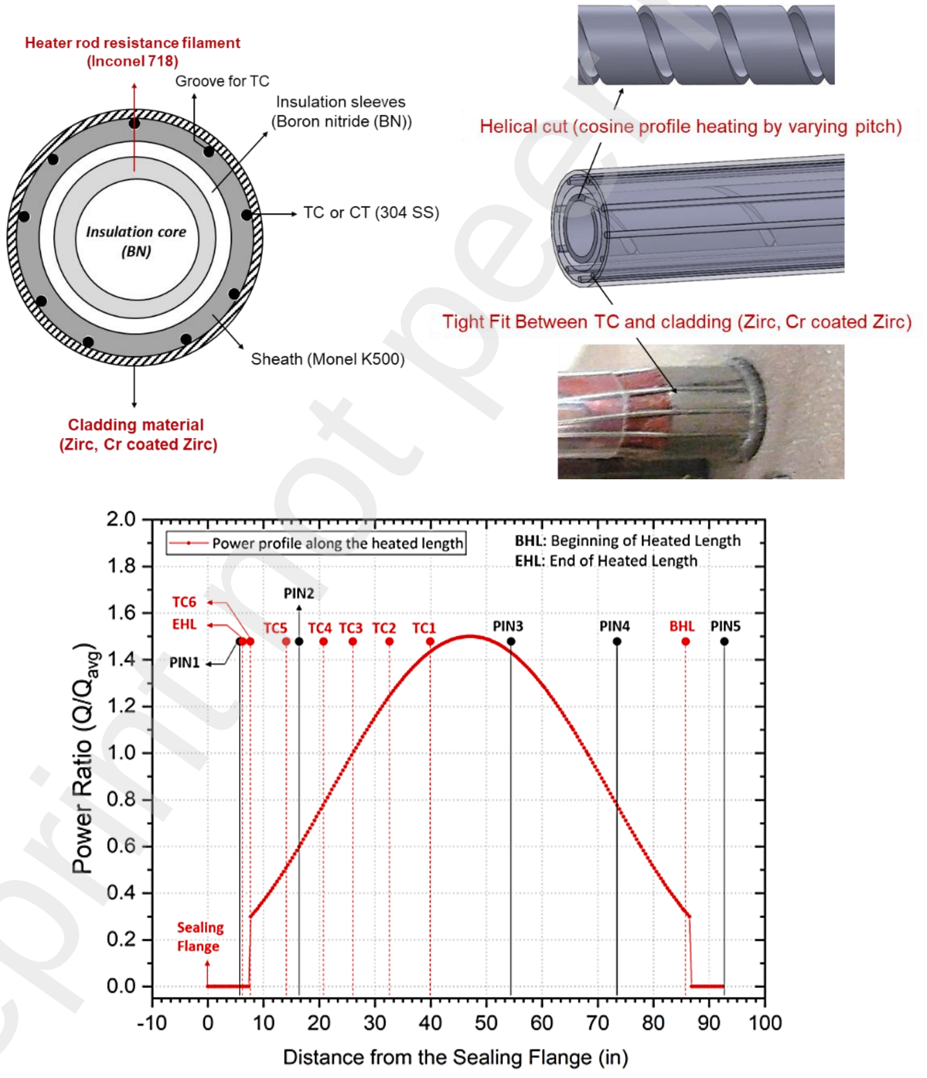

Figure 9. Schematic of the heater rod configuration and the circumferential arrangement of thermocouples (TC) and capillary tube (CT) for the optical fiber sensor (top). Axial locations of thermocouples showing the cosine heat flux profile along the heated length (bottom).

Differently from the low-pressure loop, the test section for the high-pressure loop experiments is indirectly heated. Two different claddings are used for the experiments in the high-pressure loop, one bare zircaloy and one Cr-coated zircaloy with the same surface properties as the CS-S used for the low pressure experiments. The surface properties of the two tested claddings are consistent with those for the low-pressure tests summarized in Table 2.

The heater rods are equipped with 6 K-type thermocouples and 3 optical fibers at different axial and circumferential positions, as illustrated in Figure 9 (top), to characterize and identify the correct location where the DNB starts. Precisely, the temperature threshold for the DNB detection is ~25 °C above the one at the previous steady-state heat flux step. Note that one cannot use the cladding resistivity to detect DNB, as there is no electric current circulating through the cladding. Also, the CHF may not occur at the very end of the test section (as expected for directedly-heated low-pressure experiments where the heat flux is uniform), because of the cosine-shape heat flux profile. The thermocouples are axially distributed in the downstream half of the heater rod, as shown in Figure 9 (bottom), where the DNB is expected to occur, and the optical fibers equally spaced of 120° along the rod circumference, see Figure 9 (top). The sampling rate of the optical fiber system is 100 Hz at a spatial resolution of 2.5 mm. The test procedure of these high-pressure tests is similar to the one of the low-pressure tests. The high-pressure test matrix is summarized in Table 3. These conditions are selected similar to those investigated by Wheatherhead [59].

Table 3. Nominal operating conditions for high-pressure CHF tests.

Pressure [MPa]	Mass Flux [kg/m^2/s]	Subcooling [°C]
10.3	1965	10, 30, 40
10.3	2712	10, 20, 30
15.2	1965	10, 30, 50
15.2	2712	10, 20, 30
20.0	1965	20, 30, 50
20.0	2712	20, 30, 50

Figure 10 shows a comparison between the total power delivered through the heated rod when the DNB is detected. Note that the total power is a proxy for the average surface heat flux. These results show quite convincingly that the are no practical differences between the bare and chromium coated surfaces. In some cases, the results are perfectly overlapped (i.e., it is impossible to distinguish the marker for the bare and the coated surface). Such conclusion is corroborated by the comparison between coated and uncoated surfaces proposed in Figure 11 (left). Figure 11 (right), instead, shows a comparison of the local CHF values (i.e., the heat flux at the location where DNB starts) obtained for the bare and Cr-coated heater rods. The results shown in Figure 11 are obtained from the optical fibers temperature data. The local CHF is estimated from the cosine heat flux profile (Eq. 6), considering the location of the CHF as the one associated to a temperature excursion nearest to the inlet of the test section. At a pressure of 10.3 MPa, the local CHF percentage difference, defined as the absolute difference divided by the bare zircaloy value, varies from 9.8% to 82.3%. Most tests, i.e., 6 out of 7, show slightly higher CHF for the Cr-coated heater rod. At 15.2 MPa, a reduction in the local CHF difference range occurs, ranging from 4.5% to 44.2%. The tests show either close or slightly higher CHF for the Cr-coated heater rod, see Figure 11. At the highest test pressure of 20 MPa, the local CHF difference range reduces even further, to values from 5.6% to 29.7%. Most tests, i.e., 4 out of 6, show close CHF values between the bare and Cr-coated heater rod. In summary, it can be indicated that CHFs from Cr-coated heater rods are either close to or slightly higher than the values for the bare zircaloy heater rods with an average difference of 18.8%. It is worth to highlight that, under certain conditions, different CHF location are noticed based on the optical fibers temperature data. This indicates that the dryout starts in one spot and spreads downstream. Such a phenomenon leads to an uncertainty of the local CHF estimative, possibly being the culprit for the differences shown in Figure 11 (right). More details about these high-pressure experiments can be found in a parallel communication [60].

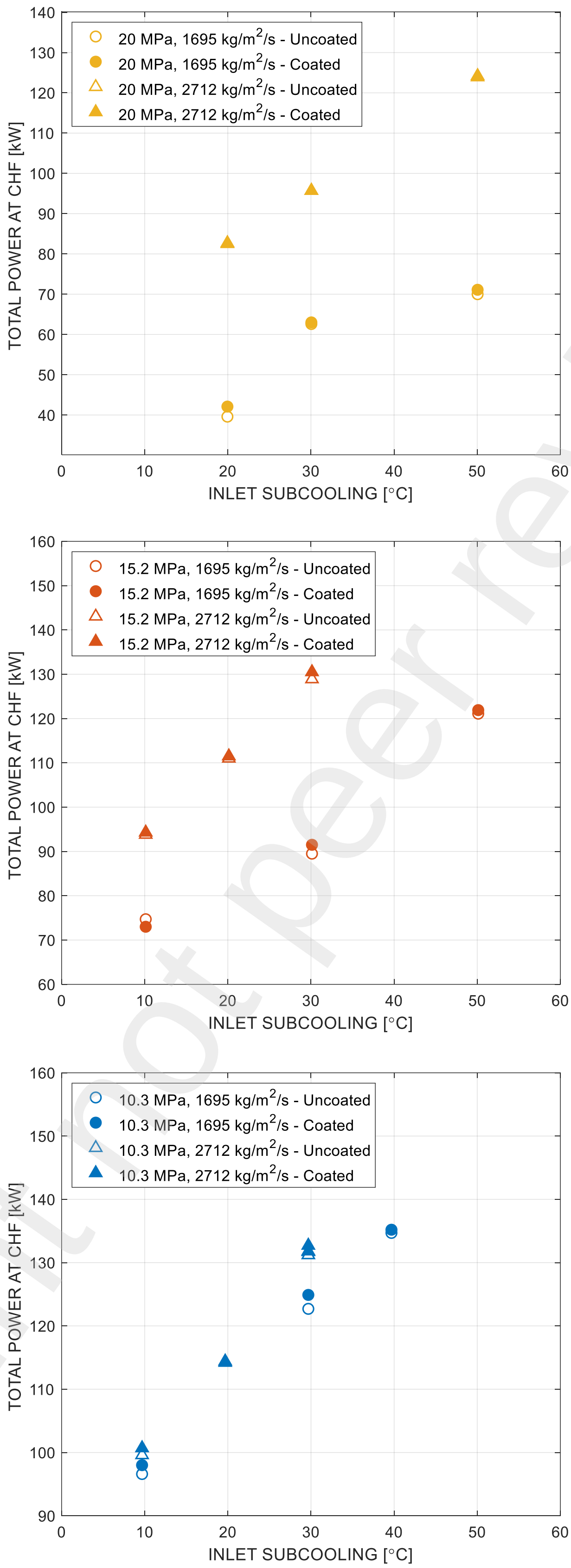

Figure 10. Comparison of total power at CHF between bare and coated heater rod: (bottom) 10.3 MPa (middle) 15.2 MPa and (total) 20 MPa nominal pressure condition.

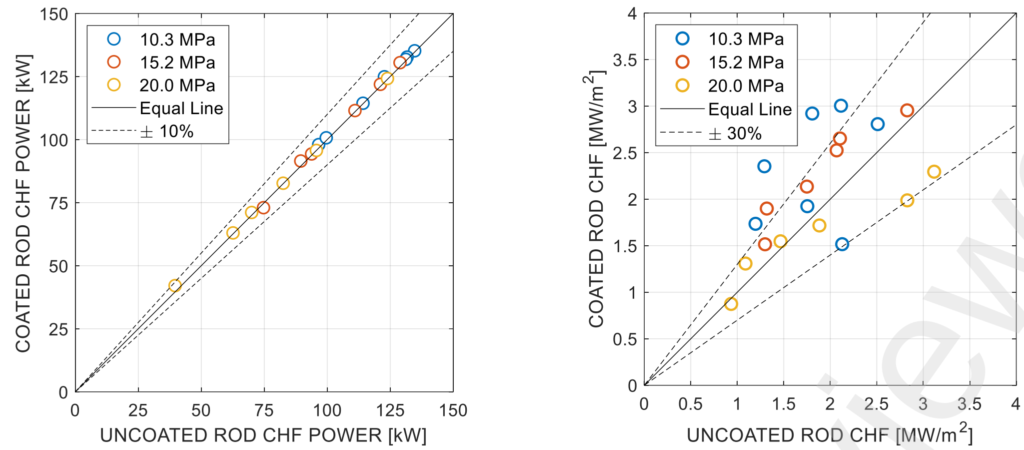

Figure 11. Comparison of local CHF (right) and total CHF Power (left) between bare and coated heater rod: (a) 10.3 MPa (b)15.2 MPa and (c) 20 MPa nominal pressure condition. Dotted lines represent the ± 30% deviation.

4.2. High-pressure flow boiling experiments with a uniform heat flux distribution

The Westinghouse Advanced Loop Tester (WALT) loop allows investigations of flow boiling DNB at prototypical PWR pressure, temperature, and water chemistry. The schematic of WALT loop is shown in Figure 12. A centrifugal pump drives the specially treated water into the autoclave from top. The water first flows downwards through the downcomer and then changes direction to flow vertically upwards through the inner chimney, which comprises the WALT loop test section. The test section features an annular flow path, which is formed by the concentric inner chimney with an ID of 20.96 mm and the heater rod with an OD of 9.5 mm. The WALT loop is capable of operating up to a 17.22 MPa system pressure, a 6 m/s linear velocity, and close to local saturation temperature at the inlet of the inner chimney. One unique capability of WALT loop is to simulate the PWR water chemistry in addition to the prototypical pressure and temperature. The coolant used during the DNB tests consists of 1000 ppm of Boric Acid, and 4 ppm of LiOH dissolved in high purity DI water, which is consistent with the PWR reactor coolant system (RCS). Hydrogen was added to the coolant at concentrations between 25 and 50 cc/kg. The WALT heater rod is shown in Figure 13. It has a total length of 445 mm, with a central heated length of 133 mm. The heater rod is connected to a DC power supply and generates by Joule effect a uniform heat flux. Four thermocouples attached to the inner surface of the heater rod (see Figure 13) are used to monitor the cladding temperature and detect the occurrence of DNB events. Two sets of heater rods, i.e., uncoated Optimized ZIRLO rods and cold spray Cr-coated Optimized ZIRLO rods, are used in these experiments. In addition, the heater rods have been coated with a simulated crud deposit to evaluate the crud effect on CHF. The crud deposits are created by adding FeEDTA, NiEDTA, and colloidal crud precursors to the WALT loop during medium heat flux boiling [49].

After the system reaches the desired system pressure, chimney inlet temperature, and mass flux, the DNB test starts from an arbitrary single-phase convective heat transfer point, with the power being gradually increased until DNB is achieved. The heat flux step increment is gradually reduced when DNB conditions are approached. The heater rod power is cut off based on the cladding temperature increasing rate. Precisely, the power shutdown occurs if the cladding temperature increases at a rate of 20 ºC per second or faster. The DNB occurrence is also confirmed by a rapid change in the rod electrical resistance, due to a rapid change of the cladding temperature. The CHF is the average heat flux at the operating condition prior to the heater rod temperature spike.

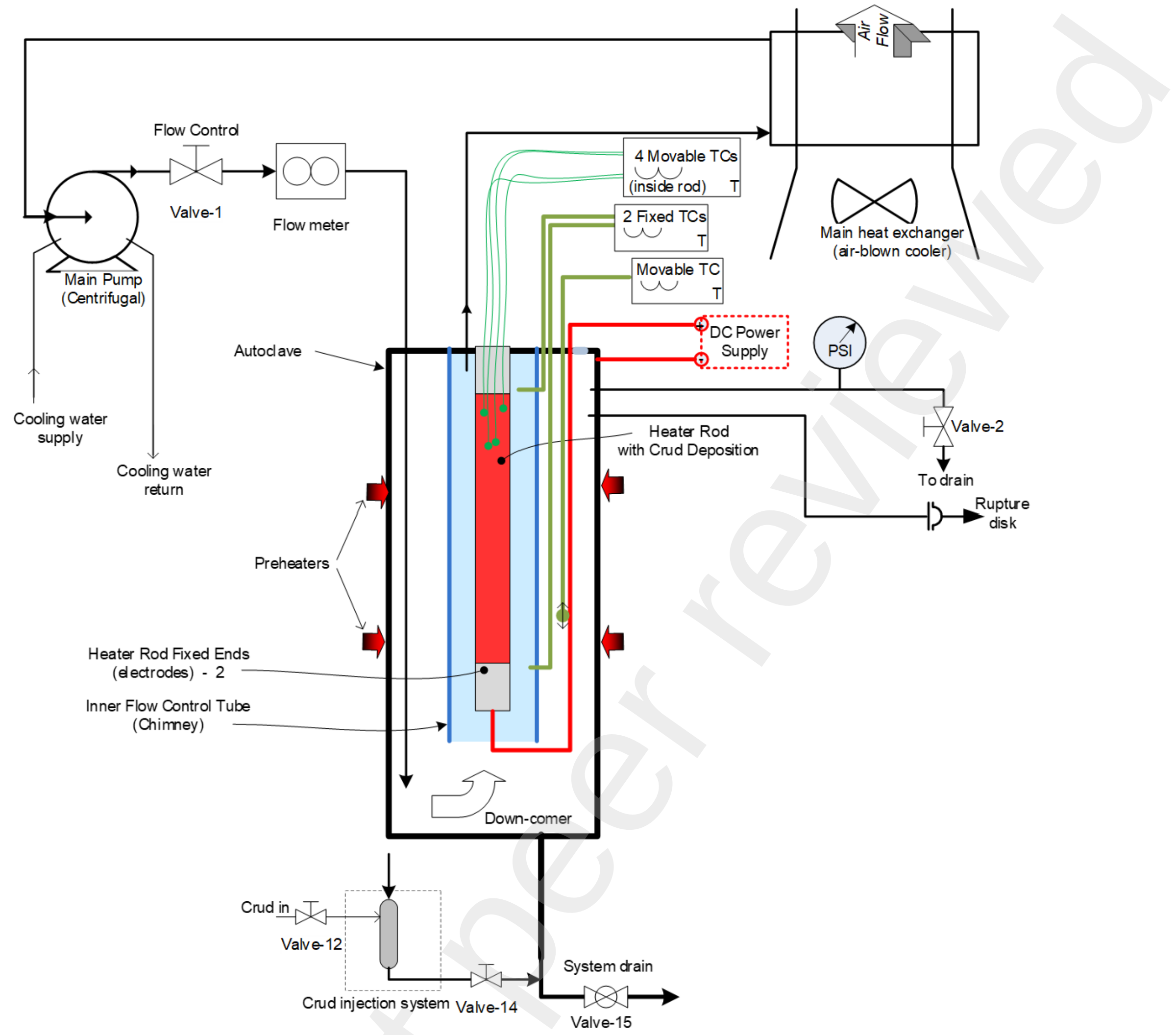

Figure 12. Schematics of WALT loop.

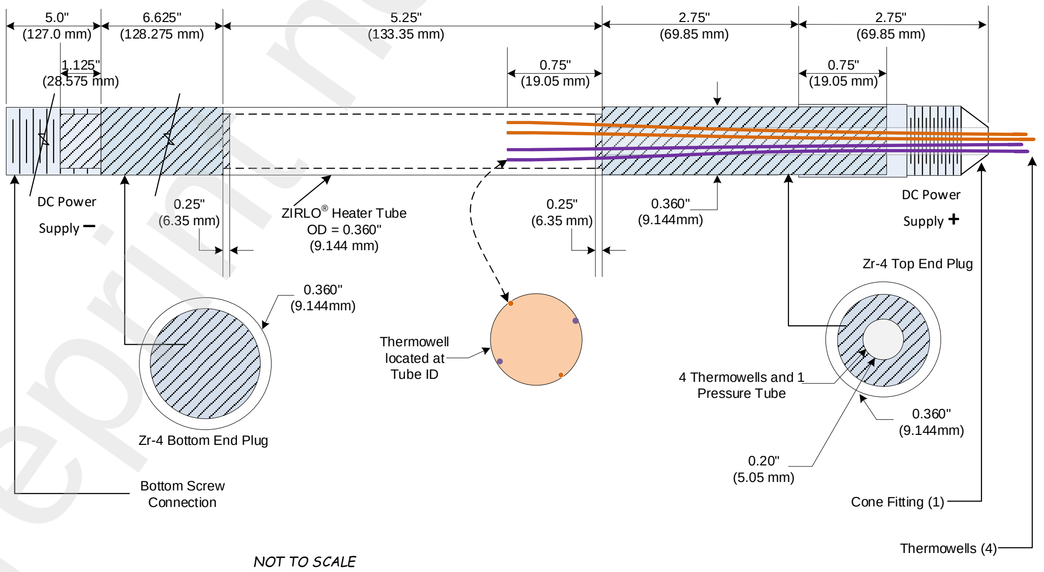

Figure 13. Sketch of WALT DNB heater rod design.

Experiments are performed for uncoated Optimized ZIRLO and Cr-coated Optimized ZIRLO rods, at a nominal system pressure of 15.5 MPa, a chimney inlet subcooling 4 °C, and a mass fluxes of 1245 kg/m^2/s. To understand better the effect of crud, test results for Cr-coated Optimized ZIRLO with crud [49] are also discussed in this analysis. The tests to evaluate the effect of CRUD were performed with a higher mass flux (2075 kg/m^2/s). The thickness of the crud deposits is about 40 µm. The repeatability of the CHF experiments is confirmed by testing different heater rods for each cladding surface condition.

CHF experimental results of the run at mass flux of 1245 kg/m^2/s are shown in Figure 14 (left). This figure shows that the CHF values for the Cr-coated Optimized ZIRLO rods are similar to those for uncoated Optimized ZIRLO rods. Assuming that the scatter of CHF values follows the t-distribution, it is possible to calculate the 95% confidence interval of the mean for uncoated and Cr-coated test results as shown in Figure 14 (right). The confidence interval of the uncoated results completely covers the confidence interval of the Cr-coated results. Practically, there is no statistical difference in the mean CHF values for uncoated and Cr-coated tests. Similar conclusion can be drawn from the result at mass flux of 2075 kg/m^2/s shown in Figure 15 (left).

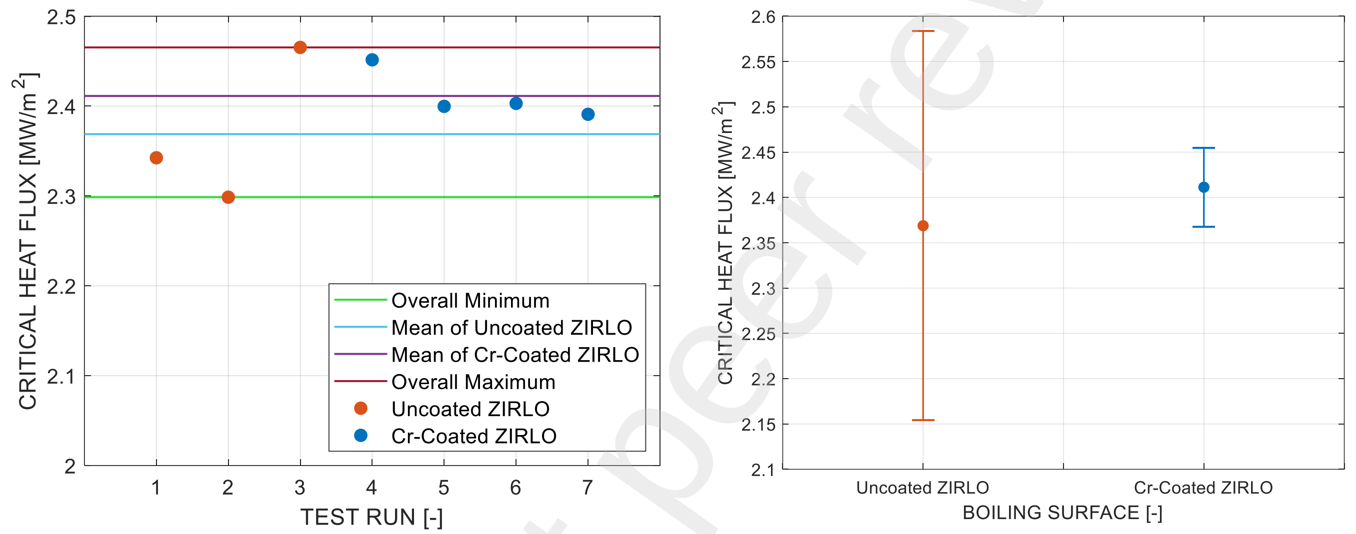

Figure 14. Comparison of CHF values (left) and confidence intervals (right) of uncoated and Cr-coated surface at a mass flux of 1245 kg/m^2/s, with 4 °Cof inlet subcooling at 15.5 MPa, obtained with the WALT loop.

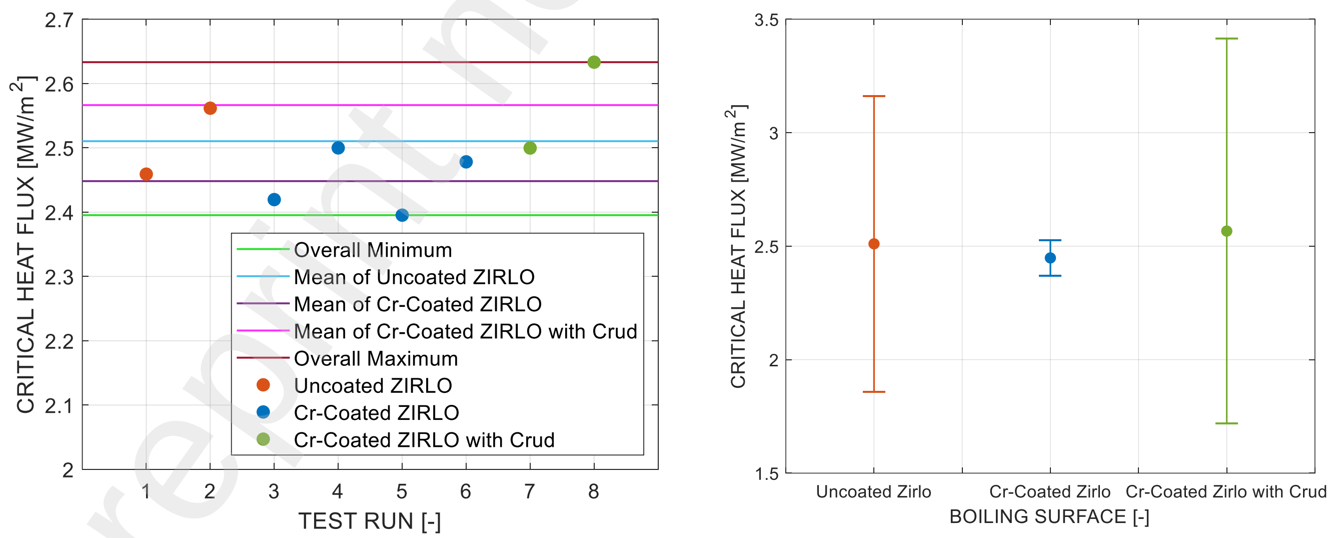

Figure 15. Comparison of CHF values (left) and confidence intervals (right) of uncoated, Cr-coated, and Cr-coated with crud surfaces at a mass flux of 2075 kg/m^2/s, with 4 °C of inlet subcooling at 15.5 MPa, obtained with the WALT loop.

Neither the Cr-coating nor the crud deposits deteriorate CHF compared to uncoated test results. The confidence interval of the uncoated results largely overlaps with the confidence interval of the Cr-coated and Cr-coated with crud results as shown in Figure 15 (right). Note that the large confidence intervals for uncoated and Cr-coated with crud results in Figure 15 (right) come from the small number of the data points rather than the scattering of the data themselves.

4.3. Post DNB metallography analyses

The microscopic structure of the uncoated and Cr-coated heater rods used in the WALT loop testing is examined at the DNB location through a Scanning Electron Microscope (SEM). The metallographic structure of the uncoated ZIRLO rods is shown in Figure 16. Oxygen rapidly penetrates the uncoated ZIRLO surface, forming a continuous brittle oxygen-stabilized alpha phase near the surface that appears brighter in the SEM image. Deeper into the cladding, there is an elongated oxygen-stabilized beta phase penetrating along the grain boundaries of metallic phase. This microstructure is typical of a zircaloy cladding heated to high temperatures in steam or water.

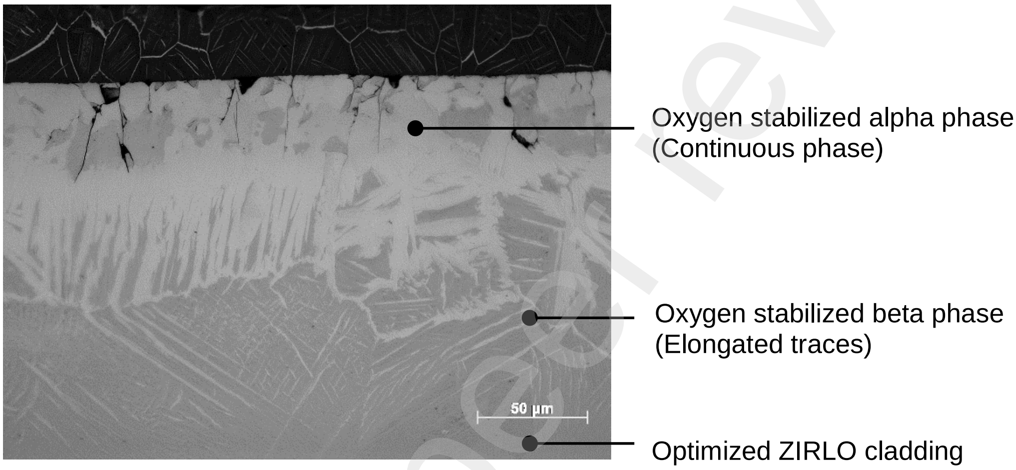

Figure 16. Metallographic structure of the uncoated ZIRLO within the DNB spot.

Different from the uncoated ZIRLO rods, the cold-sprayed Cr coatings remain well bonded to the underlying ZIRLO and protect it from excessive oxidation and cracking, as shown in Figure 17. The brittle zirconium oxide phase is inhibited as long as an intact metallic chromium layer exists. The extent of cracking in the Cr-coated cladding after DNB events is much less than in uncoated cladding. However, once all metallic chromium is converted into a Cr-Zr intermetallic phases, oxidation proceeds and cracking in the brittle oxygen-containing phases and intermetallic phases is similar to that found in uncoated ZIRLO. It is worth of mention that damages to the external surface of the rod are visually observed on the bare zircaloy rods tested in the UWM loop, whereas such damages are not visible on the Cr-coated surfaces [12].

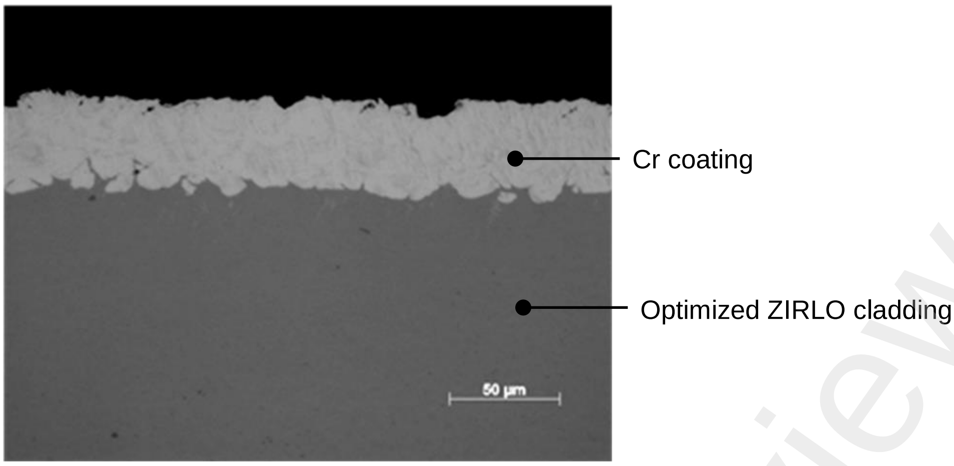

Figure 17. Metallographic structure of the Cr-coated ZIRLO within the DNB spot.

5. Transient CHF test

5.1. Flow boiling facility and infrared heaters

Transient CHF experiments are performed in subcooled flow boiling conditions with an exponentially increasing heat flux (i.e., $q'' \propto e^{t/\tau}$, where τ is the period of the power escalation), simulating the reactor power increase during a hypothetical reactivity accident. These tests are run using the MIT Pether platform. The test section features a rectangular cross-section channel (1×3 cm^2). It stands on top of a developing channel with the same cross-section, and more than 60 hydraulic diameters long to guarantee fully-developed turbulent flow at the actual test section. Each side of the test section channel has an opening (see an exploded view in Figure 18). Three sides accommodate quartz windows that provide optical access to the flow. The remaining side accommodates a Shapal^{TM} cartridge, which, in turn, houses the heating element. This heating elements enable infrared (IR) measurements of the time-dependent temperature and heat flux distribution on the boiling surface with a high temporal (0.4 ms) and spatial resolution (123 µm/pixel). Heater, cartridge, quartz windows, and test section, are all accurately flush with each other to form a rectangular channel with perfectly flat walls. The reader interested in the details of the apparatus is directed to Ref. [52].

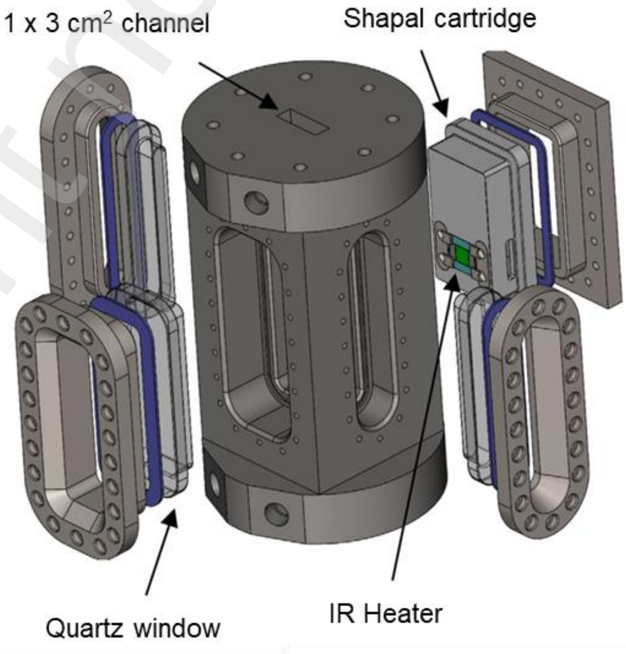

Figure 18. Exploded view of the 3D design for the flow boiling test section at MIT.

We conduct transient flow boiling experiments on a surface mimicking the chromium coated nuclear reactor cladding and compare the results to those previously obtained using a nano-smooth surface, which is supposed to have a radically different boiling behavior. The nano-smooth IR heater, and consists of a 1 mm thick sapphire substrate, coated with a 700 nm thick indium tin oxide (ITO) layer, as shown in Figure 19 left. The ITO, in contact with water, has an active heating area ~1×1 cm^2 (red treat in Figure 19 left). The ITO is very thin and has a negligible thermal resistance and heat capacity. Practically, the temperature at the sapphire-ITO interface coincides with the temperature at the ITO-water interface, i.e., the boiling surface. Importantly, the ITO layer is completely IR opaque. Thus, the radiation that it emits can be used to measure the time-dependent temperature and heat flux distributions on the boiling surface. Practically, this task requires the solution of an inverse problem coupling optical radiation and conduction heat transfer in the sapphire substrate. The reader interested in the details of this technique is directed to Refs. [40,53].

It is worth mentioning that the thermal properties of sapphire are similar to zircaloy [52]. Therefore, the thermal response of sapphire and zircaloys to a bubble life cycle is expected to be similar. In summary, the key difference between nano-smooth sapphire-ITO IR heaters and commercial-grade heating surfaces is the surface finish and wettability. In this work, we develop a new infrared heater, whose surface mimics the finish and wettability of a chromium coated fuel cladding. The new heater builds upon the same type of substrate as the nano-smooth IR heater, as shown in Figure 19 right. It features a ~4 µm thick chromium nitrate heating layer with an active heating area of ~1×1 cm^2 (red treat in Figure 19 right). Chromium nitride (CrN_x, with x = 1 to 2) is used to simulate the wettability of metallic chromium. The active CrN_x area is grinded using P360-grit sandpaper until the desired roughness and scratch pattern as the commercial surface roughness is obtained. A sufficiently thick heating element layer, i.e., ~ 4 µm, is required to survive the grinding, while still maintaining the uniform heating power distribution and negligible thermal resistance and heat capacity. Note that metallic chromium is not suitable for this purpose due to very low electric resistance at such thicknesses. The chromium nitrate layer is IR opaque. Thus, the radiation that it emits can be used to measure the time-dependent temperature and heat flux distribution on the boiling surface using the same technique used for the nano-smooth ITO heater.

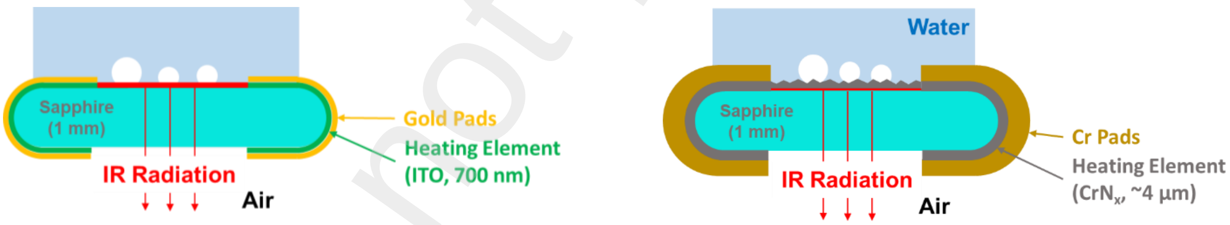

Figure 19. Sketch (not to scale) of the nano-smooth ITO IR heater (left) and the rough IR heater (right).

The nano-smooth heater preserves the crystalline smoothness of the sapphire substrate (with an Ra < 0.01 µm) except for small imperfections caused by the sapphire machining process, which may serve as nucleation sites. The rough IR heater has many parallel scratches and a much higher surface roughness (Ra~0.3 µm). The contact angle measured on nano-smooth ITO surface is 86˚ ± 3˚ in air at ambient pressure. A larger variation is noticed in the contact angle measured for the rough CrN_x surface, showing 72˚ ± 3˚ and 61˚ ± 5˚ respectively for 2 randomly selected samples.

We use the same diagnostics and data acquisition technique as the one used in Refs. [40,43], as illustrated in Figure 20.

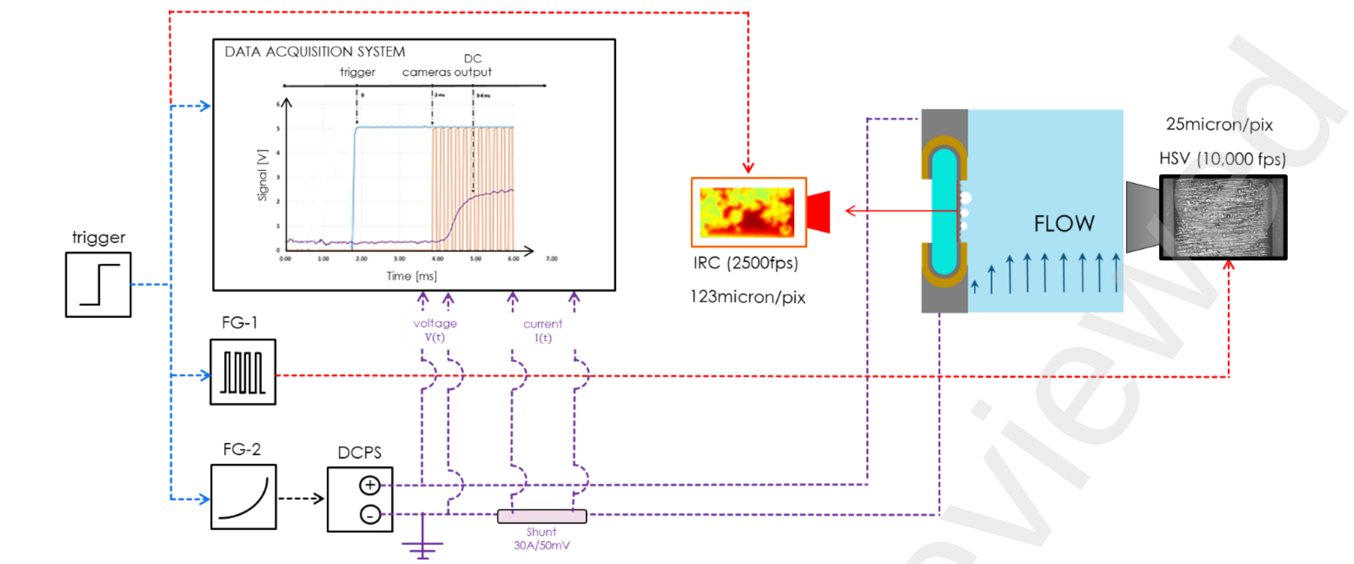

Figure 20. Schematic diagram of the measurement techniques and data acquisition system for the transient experiments.

A IRC806HS high-speed infrared (HSIR) camera captures the infrared radiation emitted by the boiling surface with a temporal resolution of 0.4 ms and pixel resolution of 123 μm. A Phantom v.12.1 high-speed video (HSV) camera driven by a function generator (FG-1) is used to capture images of the bubbles on the boiling surface. The HSV operates at an acquisition frequency of 10,000 fps and pixel resolution of 25 μm. A second function generator (FG-2) is used to drive the exponential output of the DC power supply (DCPS). The voltage and current are measured with an Agilent U2542A high speed data acquisition system (HSDAS). At the beginning of each test, the HSIR camera, HSDAS, FG-1 and FG-2 are simultaneously initialized with a single trigger signal. Further, a controlled delay between the trigger and outputs of FG-1 and FG-2 to capture the beginning of the transient is introduced.

The experiments consist in exponentially increasing the heat flux released by the heating element according to the desired power escalation period τ. Experiments are conducted in ambient pressure, with 50 °C of subcooling, and mass flux of 1275 kg/m^{2}s, which corresponds to a Reynolds number of 35000. The power escalation periods covered in the campaign vary from 5 milliseconds to 500 milliseconds. CHF is defined as the value of heat flux that creates the first irreversible dry spot on the boiling surface, which is the same criterion used in Ref. [43]. The identification of such conditions is possible thanks to the infrared measurements. An irreversible dry spot is such that it never gets rewetted once it appears on the boiling surface (unless there is a reduction of the applied heat flux). The reported CHF in this study is the average heat flux transferred to water at the moment when the first irreversible dry spot starts to grow on the surface. Details about the procedure to estimate the uncertainty on the measured CHF values are discussed in Ref. [43]. Briefly, the overall uncertainty is determined by three main contributions: the measurement uncertainty of the applied heat flux that is propagated from voltage and current measurement; the absolute temporal uncertainty that depends on the frame rate of the IR camera; and the standard deviation of CHF values measured in different runs.

The measured transient CHF values for the rough CrN_x heater are shown in Figure 21, compared to the values measured on the nano-smooth heater under the same exact operating conditions [43]. Two clear asymptotic regions emerge from the plot. The first asymptotic region, Asymptotic Region I, is observed for slow transients (i.e., large exponential power escalation periods with $\tau >$ ~100 ms). The CHF values plateau for both heaters. Under such conditions, the boiling process is practically the same as observed with steady-state heat flux inputs. The second asymptotic region, Asymptotic Region II, corresponds to fast transients (i.e., small power escalation periods with $\tau <$ ~10 ms). In this case, the CHF increases with decreasing periods (precisely, it is proportional to $1/\sqrt{\tau}$). However, while the CHF for the two different surfaces are, as expected, different under steady-state conditions (i.e., Asymptotic Region I), they converge to similar values as the period is shortened (i.e., Asymptotic Region II).

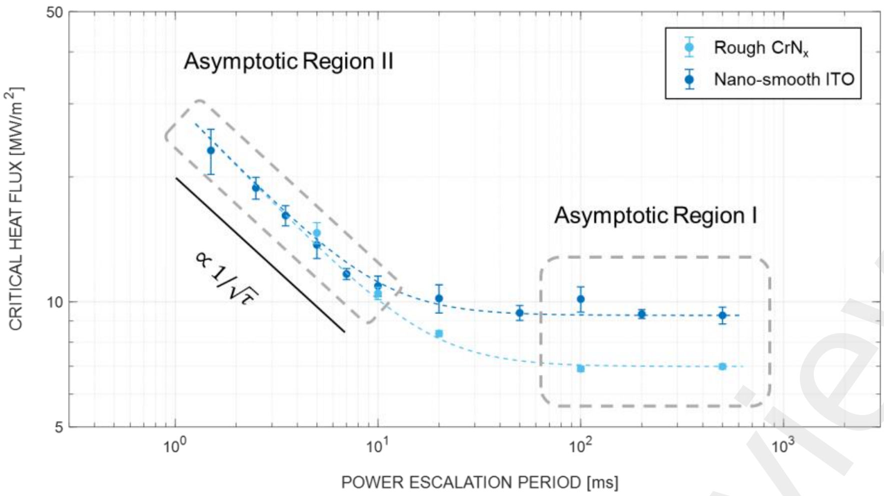

Figure 21. Transient CHF versus power escalation period for rough CrNx and nano-smooth ITO surfaces. The grey dashed-line boxes indicate two asymptotic regions. The black solid line shows a reference trend of $\propto 1/\sqrt{\tau}$.

At long periods (with τ > ~100 ms), the CHF is independent of the exponential escalation period. Under high subcooling conditions, such as the ones in the present tests, bubble growth is limited by the relatively thin superheated liquid layer adjacent to the wall. Bubbles condense whenever they grow beyond the superheated layer. As already reported in several studies [54-58], the CHF during steady state conditions depends on surface conditions, such as roughness and morphology. The difference in surface condition changes bubble parameters, such as nucleation site density, bubble radius, and, therefore, the way they interact with each other [58]. As a result, the CHF may be different. As observed in Figure 21, for Asymptotic Region I, the measured CHF value for the rough heater is about 75% of the value for nano-smooth heater at 500 ms transient power input. Such difference is consistent with the findings of our previous study with steady-state heat inputs [58].

Several studies attempt to model and quantify the transient CHF based on a presumed triggering mechanism of the steady state CHF [34,35,59]. In these studies, the boiling crisis triggering mechanism for transient or steady state boiling is assumed to be the same, no matter how fast is the transient, and the transient CHF value is predicted by multiplying the steady state CHF value with a scaling factor dependent on the power escalation period. The implication of this assumption is that, given different steady state CHF values for different surface conditions, the CHF values at short periods should also be different, since the proposed scaling factor is the same regardless of the surface conditions. In other words, one should expect the light blue dots in Asymptotic Region II of Figure 21 to be in a parallel asymptote, lower than the one for the dark blue dots. Clearly, this prediction is in contradiction with the present data: the CHF measurements for the two different boiling surfaces overlap with each other in Asymptotic Region II, as shown in Figure 21. These results suggest that there is a decorrelation between the steady state and the transient CHF mechanisms, questioning the theoretical basis and the validity of mechanistic models and correlations that aim to predict the transient CHF from steady state value, as discussed before. In addition, it is plausible that the boiling crisis mechanism for fast transient is different from the one under steady state conditions. The relative importance of different physical phenomena may change with power escalation periods. Surface effects, which are key parameters in the prediction of the CHF under steady-state conditions, seems to diminish at fast transient power escalations. CHF trends for different surfaces show the same dependency on the period for fast transient, i.e., inversely proportional to the square root of period ($\propto 1/\sqrt{\tau}$), as shown in Figure 21 and also reported in Ref. [43]. Such dependency is the same as the heat transfer coefficient for single-phase transient conduction. This observation suggests that transient conduction in the liquid may be the limiting heat transfer mechanism in fast transient conditions. In conclusion, while further investigations are necessary to consolidate these findings, it is plausible that chromium coatings and other surface effects do not negatively affect the transient CHF under rapid power escalation conditions.

6. Conclusion

Chromium-coated nuclear reactor fuel claddings can resist runaway steam oxidation under extreme temperature (> 1200 ℃) and retain their mechanical strength and structural integrity under thermal shocks. They have the potential to replace conventional zircaloy claddings. However, it is necessary to demonstrate that the chromium coating does not deteriorate the CHF limit compared to conventional zircaloy claddings, in particular in high-pressure operating conditions.

In this paper, we present the results of a collaborative research effort aimed at evaluating the thermal-hydraulics performance of chromium-coated zircaloy claddings. We have developed experimental facilities and conducted experiments to measure the wettability of chromium coated and convention zircaloy cladding materials in vapor-saturated atmosphere from ambient pressure up to the operating pressure of PWRs, as well as the flow boiling CHF limit at near-atmospheric pressure and at pressures close to PWR conditions. The high-pressure flow boiling CHF tests were conducted with a uniform heat flux and a cosine-shape heat flux profile, and exploring (for the uniform heat flux tests) the effect of CRUD deposits on the cladding surface. Our results demonstrate that the chromium coating does not deteriorate the CHF limit of conventional zircaloy claddings, not even when covered by a CRUD deposit. Instead, the chromium coating improves significantly the post-CHF behavior, as the it prevents the reaction between zircaloy and steam, which results in the formation of a brittle zirconium oxide through the surface of the cladding. We also conducted transient CHF under exponentially escalating heat flux inputs. The results of these transient heat flux tests suggest that the CHF limit for very short periods (i.e., fast transients) is independent of the surface finish, being the same for a rough chromium surface or a nano-smooth surface.

Future research will focus on consolidating the results of the transient CHF tests under exponential power escalations, as well as anticipated operational occurrences (e.g., a power pulse during a BWR turbine trip), post-LOCA reflooding scenarios, and post-CHF heat transfer at ambient pressure and PWR conditions.

Acknowledgments

This material is based upon work supported by U.S. Department of Energy Office of Nuclear Energy's Nuclear Energy University Program (NEUP).

CRediT authorship contribution statement

G. Su: Conceptualization, Methodology, Investigation, Visualization, Formal analysis, Writing - Original Draft. **T. A. Moreira:** Conceptualization, Methodology, Investigation, Visualization, Formal analysis, Writing - Review & Editing. **D. Lee:** Conceptualization, Methodology, Investigation, Visualization, Formal analysis. **A. Jena:** Investigation, Visualization, Formal analysis. **G. Wang:** Investigation, Visualization, Formal analysis, Writing - Review & Editing. **A. Byers:** Investigation, Visualization, Formal analysis. **B. Phillips:** Conceptualization, Methodology, Investigation, Supervision. **Z. Karoutas:** Investigation, Visualization, Formal analysis, Funding acquisition, Writing - Review & Editing. **M. Anderson:** Conceptualization, Methodology, Formal analysis, Funding acquisition, Supervision, Writing - Review & Editing. **M. Bucci:** Conceptualization, Methodology, Formal analysis, Funding acquisition, Supervision, Project administration, Writing - Review & Editing.

References

[1] S. Bragg-Sitton, “Development of advanced accident-tolerant fuels for commercial LWRs”, Nucl. News, 57 (2014) 83-91.

[2] M. Kazimi, and K. Shirvan, "Development of Accident Tolerant Fuel Options For Near Term Applications", United States, 2019, https://www.osti.gov/servlets/purl/1512924.

[3] M. T. Farmer, et. al., “Scoping assessments of ATF impact on late-stage accident progression including molten core–concrete interaction”, J. Nucl. Materials, 448 (2014) 534-540.

[4] K. A. Terrani, “Accident tolerant fuel cladding development: Promise, status, and challenges”, J. Nucl. Materials, 501 (2018) 13-30.

[5] X. Han, et. al., “Oxidation behavior of FeCrAl coated Zr-4 under high temperature steam environment”, Corros. Sci., 149 (2019) 45–53.

[6] N. E. Todreas and M. S. Kazimi, Nuclear Systems – Volume 1, Taylor and Francis (2012).

[7] G. H. Seo, G. Jeun, and S. J. Kim, “Pool boiling heat transfer characteristics of zircaloy and SiC claddings in deionized water at low pressure”, Exp. Therm. Fluid Sci., 64 (2015) 42–53.

[8] G. H. Seo, G. Jeun, and S. J. Kim, “Enhanced pool boiling critical heat flux with a FeCrAl layer fabricated by DC sputtering”, Int. J. Heat Mass Transf. 102 (2016) 1293–1307.

[9] H.H. Son, et. al., “Capillary wicking effect of a Cr-sputtered superhydrophilic surface on enhancement of pool boiling critical heat flux”, Int. J. Heat Mass Trans., 113 (2017) 115–128.

[10] H.J. Jo, et. al., “Evaluation of critical heat flux of ATF candidate coating materials in pool boiling”, Nucl. Eng. Des. 354 (2019) No. 110166.

[11] S.K. Lee, et. al., “Comparison of steady and transient flow boiling critical heat flux for FeCrAl accident tolerant fuel cladding alloy, Zircaloy, and Inconel, Int. J. Heat Mass Trans. 132 (2019) 643–654.

[12] D. Lee, et. al., “Enhanced flow boiling heat transfer on chromium coated zircaloy-4 using cold spray technique for accident tolerant fuel (ATF) materials”, App. Thermal Eng. 183 (2021) No. 116347.

[13] M. Maracy and R. Winterton, “Hysteresis and contact angle effects in transition pool boiling of water,” Int. J. Heat Mass Trans., 31 (1988) 1443-1449.

[14] J. Ramilison, P. Sadasivan and J. Lienhard, “Surface factors influencing burnout on flat heaters,” J. Heat Transfer, 114 (1992) 287-290.

[15] S. Kandlikar, “A theoretical model to predict pool boiling CHF incorporating effects of contact angle and orientation,” J. Heat Trans., 123 (2001) 1071-1079.

[16] S. Kim, I. Bang, J. Buongiorno and L.-W. Hu, “Surface wettability change during pool boiling of nanofluids and its effect on critical heat flux,” Int. J. Heat Mass Trans., 50 (2007) 4105-4116.

[17] L. Liao, R. Bao and Z. Liu, “Compositive effects of orientation and contact angle on critical heat flux in pool boiling of water,” Heat Mass Transfer, 44 (2008) 1447-1453.

[18] M. Phillips and A. Riddiford, “Temperature dependence of contact angles,” Nature, 205 (1965) 1005-1006.

[19] H. Schonhorn, “Dependence of contact angles on temperature: polar liquids on polyethylene,” Nature, 210 (1966) 896-897.

[20] J. Jones and A. Adamson, “Temperature dependence of contact angle and of interfacial free energies in the naphthalene-water-air system,” Journal of Physical Chemistry, 72 (1968) 646-650.

[21] A. Ponter and A. Boyes, “Temperature dependence of contact angles of water on a low energy surface under conditions of condensation and at reduced pressures,” Nature Physical Science, 231 (1971) 152-153.

[22] A. Boyes and A. Ponter, “Wettability of copper and polytetrafluoroethylene surfaces with water - the influence of environmental conditions,” Chemie Ingenieur Technik, 45 (1973) 1250-1256.

[23] M. Yekta-Fard and A. Ponter, “The influences of vapor environment and temperature on the contact angle-drop size relationship,” Journal of Colloid and Interface Science, 126 (1988) 134-140.
[24] A. F. Ali, et. al., “Surface wettability and pool boiling Critical Heat Flux of Accident Tolerant Fuel cladding-FeCrAl alloys,” Nuclear Engineering and Design, 338 (2018) 218-231.
[25] J. Bernardin, I. Mudawar, C. Walsh and E. Franses, “Contact angle temperature dependence for water droplets on practical aluminum surfaces,” International Journal of Heat and Mass Transfer, 40 (1997) 1017-1033.
[26] Y. Hirose, et. al., “Experimental study on contact angle of water droplet in high-temperature condition”, Proceedings of the 14th International Conference on Nuclear Engineering, Miami, Florida, USA, 2006.
[27] J.-W. Song, D.-L. Zeng and L.-W. Fan, “Temperature dependence of contact angles of water on a stainless steel surface at elevated temperatures and pressures: In situ characterization and thermodynamic analysis,” Journal of Colloid and Interface Science, 561 (2020) 870-880.
[28] R. Kommajosyula, “Development and assessment of a physics-based model for subcooled flow boiling with application to CFD”, Doctoral Thesis, Massachusetts Institute of Technology (2020).
[29] J.R. Dietrich, D.C. Layman , “Transient and Steady State Characteristics of a Boiling Reactor”. The BORAX Experiments, Lemont (1954).
[30] M.W. Rosenthal and R.L. Miller , “An Experimental Study of Transient Boiling”, Tennessee, Oak Ridge, 1957 .
[31] H.A. Johnson, “Transient boiling heat transfer to water”, Int. J. Heat Mass Transf. 14 (1) (1971) 67–82.
[32] A. Sakurai , M. Shiotsu , “Transient Pool Boiling Heat Transfer Part 2: boiling Heat Transfer and Burnout”, J. Heat Transfer 99 (1977) 547–553 .
[33] I. Kataoka , A. Serizawa , A. Sakurai , “Transient boiling heat transfer under forced convection”, Int. J. Heat Mass Transf. 26 (4) (1983) 583–595 .
[34] K.O. Pasamehmetoglu , R.A. Nelson , F.S. Gunnerson , “Critical Heat Flux Modeling in Pool Boiling for Steady-State and Power Transients”, J. Heat Transfer 112 (4) (1990) 1048 .
[35] K.O. Pasamehmetoglu , R.A. Nelson , F.S. Gunnerson , “Critical Heat Flux model- ing in Forced Convection Boiling During Power Transients”, J. Heat Transfer 112 (1990) 1058–1062 .
[36] J. Papin , M. Balourdet , F. Lemoine , F. Lamare , J.M. Frizonnet , F. Schmitz , “French Studies on High-Burnup Fuel Transient Behavior Under RIA Conditions”, Nucl. Saf. 37 (1996) 289–327.
[37] A. Sakurai, “Mechanisms of transitions to film boiling at CHFs in subcooled and pressurized liquids due to steady and increasing heat inputs”, Nucl. Eng. Des., 197 (2000) No. 3.
[38] J. Park , K. Fukuda , Q. Liu , “Transient CHF Phenomena Due to Exponentially Increasing Heat Inputs”, Nucl. Eng. Technol. 41 (9) (2009) 1206–1214.
[39] R. Visentini , C. Colin , P. Ruyer , “Experimental investigation of heat transfer in transient boiling”, Exp. Therm. Fluid Sci. (2014).
[40] G.-Y. Su , M. Bucci , T. Mckrell , J. Buongiorno , “Transient boiling of water un- der exponentially escalating heat inputs. Part I: pool boiling”, Int. J. Heat Mass Transf. 96 (2016) 667–684.
[41] G.-Y. Su , M. Bucci , T. McKrell , J. Buongiorno , “Transient boiling of water under exponentially escalating heat inputs. Part II: flow boiling”, Int. J. Heat Mass Transf. 96 (2016) 685–698.
[42] H. Takiguchi , M. Furuya , T. Arai , K. Shirakawa , “Transient boiling flow in 5 ×5 rod bundle under non-uniform rapid heating”, Nucl. Eng. Des. 340 (2018) 447–456.
[43] A. Kossolapov, et. al., “The boiling crisis of water under exponentially escalating heat inputs in subcooled flow boiling at atmospheric pressure”, Int. J. Heat Mass Transf. 160 (2020) 120137.

[44] M. Bucci, J. Buongiorno, and M. Bucci, “The not-so-subtle flaws of the force balance approach to predict the departure of bubbles in boiling heat transfer”, Physics of Fluids, 33(1) (2021) p.017110.
[45] A. Kossolapov, M. Bucci, T. McKrell and J. Buongiorno, “Measurement of the Apparent Contact Angle of Water on Reactor Materials at Elevated Pressures and Temperatures,” in 17th International Topical Meeting on Nuclear Reactor Thermal Hydraulics, Xi'an, China, 2017.
[46] A. Neumann, “Contact angles and their temperature dependence: thermodynamic status, measurement, interpretation and application,” Advances in Colloid and Interface Science, 4 (1974) 105-191.
[47] A. W. Neumann, R. David and Y. Zuo, Applied Surface Thermodynamics, 2nd Ed., Boca Raton: CRC Press, Taylor and Francis Group, 2011.
[48] A. Adamson, “Potential distortion model for contact angle and spreading. II. Temperature dependent effects,” Journal of Colloid and Interface Science, 44 (1973) 273-281.
[49] R. H. a. M. O'Sullivan, Fiber Optic Measurement Techniques, Burlington: Elsevier, 2009.
[50] R. V. Umretiya, et. al., “Mechanical and chemical properties of PVD and cold spray Cr-coatings on Zircaloy-4”, Journal of Nuclear Materials, 541 (2020) No. 152420.
[51] Z. Karoutas, G. Wang, and W. A. Byers, “Critical heat flux and crud walt loop measurements for westinghouse accident tolerant fuel”, Top Fuel 2019, Seattle, WA, September 22-27, 2019.
[52] A. Richenderfer, et al. , “Investigation of subcooled flow boiling and CHF using high-resolution diagnostics”, Exp. Therm. Fluid Sci., 99 (2018) 35-58.
[53] M. Bucci, et. al., “A mechanistic IR calibration technique for boiling heat transfer investigations”, Int. J. Multiph. Flow, 83 (2016) 115-127.
[54] K.-H. Chu, et al., “Hierarchically structured surfaces for boiling critical heat flux enhancement”, Appl. Phys. Lett., 102 (2013) 151602.
[55] N. S. Dhillon, J. Buongiorno, K. K. Varanasi, “Critical heat flux maxima during boiling crisis on textured surfaces”, Nat. Commun., 6 (2015) 8247.
[56] M. Tetreault-Friend, et al., “Critical heat flux maxima resulting from the controlled morphology of nanoporous hydrophilic surface layers”, 108 (2016) 243102.
[57] C. Wang, et al., “Enhancement of pressurized subcooled flow boiling chf with nano-engineered surfaces”, NURETH-18, Portland, Oregon, USA, August 18-23, 2019.
[58] G.-Y. Su, et. al., “Investigation of flow boiling heat transfer and boiling crisis on a rough surface using infrared thermometry”, Int. J. Heat Mass Trans., 160 (2020) No. 120134.
[59] R. J. Weatherhead, “Nucleate boiling characteristics and the critical heat flux occurrence in subcooled axial-flow water systems”, No. ANL-6675, Argonne National Lab, 1963.
[60] D. Lee, T.A. Moreira, M. Anderson, “Critical heat flux of water on zircaloy and accident tolerant fuel materials under PWR prototypical conditions,” App. Thermal Eng. (under review).